Ceramics International 44 (2018) 17681–17687

Contents lists available at ScienceDirect

Ceramics International

journal homepage: www.elsevier.com/locate/ceramint

Structural, mechanical, thermal and optical properties of Yb, Pr-doped $Y_4Zr_3O_{12}$ ceramics

Federico González[a,b,*], Rigoberto López-Juárez[c], Hector D. Orozco-Hernández[d], Juan Zarate-Medina[d], Rabindra Khadka[a], John Collins[e], Baldassare Di Bartolo[a]

[a] Department of Physics, Boston College, 02467 Chestnut Hill, MA, USA
[b] Departamento de Ingeniería de Procesos e Hidráulica, Universidad Autónoma Metropolitana-Iztapalapa, A.P. 55-534, 09340 Ciudad de México, Mexico
[c] Unidad Morelia del Instituto de Investigaciones en Materiales, Universidad Nacional Autónoma de México, Antigua Carretera a Pátzcuaro No. 8701, Col. Ex Hacienda de San José de la Huerta, C.P. 58190 Morelia, Michoacán, Mexico
[d] Instituto de Investigaciones Metalúrgicas y Materiales, UMSNH, Edificio U, Ciudad Universitaria, Santiago Tapia 403, Colonia Centro, 58030 Morelia, Mexico
[e] Department of Physics, Wheaton College, 02766 Norton, MA, USA

ARTICLE INFO

Keywords:
Yttrium-zirconium oxide
Trivalent lanthanides
Polymerizable complex method
Thermal barrier materials
White light
IR laser irradiation

ABSTRACT

In the present work, $Y_4Zr_3O_{12}$ bulk ceramics doped with Yb^{3+} and Pr^{3+} were characterized to assess their structural, mechanical, thermal and optical properties. Specimens were synthesized by the polymerizable complex method and sintered as pellets at 1550 °C for 2 h. Samples were analyzed by X-ray diffraction (XRD), scanning electron microscopy (SEM), Vickers-indentation method, thermodilatometry, laser flash method, diffuse reflectance and luminescence spectroscopies. All compositions exhibit cubic like-fluorite structure, low thermal conductivity, moderate fracture toughness and thermal expansion coefficient values comparable to those of other yttria-stabilized zirconias. Regarding the optical properties, diffuse reflectance spectra support the oxidation of praseodymium from Pr^{3+} to Pr^{4+} in the Pr-doped specimens. When irradiated under an IR laser (975 nm), only the pellet containing Yb^{3+} showed white light emission at low and room pressures, but not the undoped, and those pellets doped or codoped with Pr. These results demonstrate that it is possible to produce white light not only in nanostructured systems but also in bulk ceramic oxides, and that the introduction of additional electronic states within the band gap of the host associated with the Pr, inhibits the generation of the white light.

1. Introduction

Compositions of the ZrO_2-Y_2O_3 solid-solution, better known as yttria stabilized zirconias (YSZ), possess remarkable physical properties, making them suitable for a wide range of technological applications such as electrolytes in solid oxide fuel cells [1] and thermal barrier coatings (TBC) [2,3]. Among the three polymorphs of ZrO_2, namely, monoclinic, tetragonal and cubic, the last one, being isostructural with fluorite, is strongly stabilized relative to the other two by the addition of Y^{3+}, and dissolves up to about 70 mol% Y^{3+} [4]. At around 57 mol% Y^{3+} it has been confirmed the $Y_4Zr_3O_{12}$ intermediary phase, with nominal composition $Y_4Zr_3O_{12}$, and forming an ordered rhombohedral structure [5,6].

YSZ are used as TBC because they have low thermal conductivities, which originate from the chemical disorder induced when Zr^{4+} is replaced by Y^{3+} [7]. Apart from the low thermal conductivity, TBC may have similar thermal expansion coefficient as those of the substrate and the bond coats, and suitable mechanical properties as well as good fracture toughness. Despite the importance of the concurrent presence of these features in TBC, their mechanical properties are not as frequently reported as the thermal properties are.

On the other hand, the generation of white-light (WL) in nanostructured materials under near infrared (NIR) laser irradiation is an active subject of research. So far, the most prominent materials in which this WL is produced, are undoped [8–11], and doped oxides [8,11–19] or containing stoichiometric concentrations of lanthanide ions [11,20–26]. We recently demonstrate this phenomenon in Yb-doped $Y_4Zr_3O_{12}$ powders [19]. Despite all these reports, many questions remain still open about the processes that give rise to this peculiar white-light emission. Among others, it is not clear: 1) what is the mechanism allowing the transformation of a narrow light-band, such as that one of a laser into a continuous broad emission band proper to thermal radiation; 2) when lasers used to stimulate the white light emission can efficiently excite the Yb^{3+} (e.g. 975 nm, 980 nm) what is

* Corresponding author at: Department of Physics, Boston College, 02467 Chestnut Hill, MA, USA.
E-mail addresses: garciaqa@bc.edu, fgg@xanum.uam.mx (F. González).

https://doi.org/10.1016/j.ceramint.2018.06.232
Received 19 May 2018; Received in revised form 27 June 2018; Accepted 27 June 2018
Available online 28 June 2018

the role played in that mechanism by the Yb^{3+}; and 3) whether the generation of white light takes place exclusively in nanostructured systems.

To assess the physical properties of YSZ, in this work we present measurements of the mechanical, thermal and optical properties of a series of cubic (Pr, Yb)-doped $Y_4Zr_3O_{12}$ bulk-ceramic pellets. The pellets were also irradiated with a 975-nm laser in order to get additional insight into those open questions related to the generation of white-light stimulated by NIR lasers.

2. Experimental

2.1. Synthesis and sintering of ceramic samples

In this work the polymerizable complex method was used for the preparation of $Y_{4-(x+y)}Pr_xYb_yZr_3O_{12}$ (hereafter YZO for $Y_4Zr_3O_{12}$ and YZO-Pr_xYb for those containing Pr^{3+} and Yb^{3+}) ceramics. The raw materials used were yttrium (III) nitrate hexahydrate (99.8%), zirconium (IV) oxynitrate hydrate (99%), praseodymium (III) nitrate pentahydrate (99.9%), ytterbium (III) nitrate hexahydrate (99.9%), citric acid, ethylene glycol and deionized water. An aqueous solution was prepared by dissolving the required amount of zirconium oxynitrate, yttrium nitrate, and ytterbium or praseodymium nitrates. This solution was stirred for 30 min, and then citric acid and ethylene glycol were added. The solution was kept at 70 °C for evaporating the solvent excess and to produce viscous solution. For promoting polymerization, the temperature was set at 90 °C. The resin was then transferred to an oven for a heat treatment at 300 °C for 30 min. Then, the pre-calcined powders were heat treated at 700 °C for 1 h. The calcined powders were uniaxially pressed at 300 MPa into disks of 13 mm in diameter and 2 mm in thickness. The pellets were sintered in air at 1550 °C for 2 h.

2.2. Structural and morphological characterization

The X-ray diffractograms (XRD) of the samples were measured in air and at room temperature using a Bruker D-8 Advance diffractometer with the Bragg-Brentano θ-θ geometry, Cu Kα radiation with a Ni 0.5% Cu–Kβ filter in the secondary beam, and a one-dimensional position-sensitive silicon strip detector (Bruker, Lynxeye). The diffraction intensity as a function of 2θ angle was measured between 15° and 75°, with a 2θ step of 0.010208°, for 38.4 s per point. Crystalline structures were refined using the Rietveld method by using the fundamental parameters approach [27] during the refinements, as implemented in the TOPAS Academic code, version 6. SRM-NIST 660 b (LaB_6) [28] was used to model the contributions of the instrument to the X-ray diffraction patterns. The parameters used in the refinements included polynomial terms for modeling of the background, the lattice parameters, terms indicating the position and intensity of the “tube tails”, specimen displacement, structural parameters, and the width of a Lorentzian profile for modeling the average crystallite size. This last feature was modeled in reciprocal space with a symmetrized harmonics expansion [29]. The standard deviations, given in parentheses in the text, show the variation in the last digit of a number; when they correspond to Rietveld refined parameters. Scanning Electron Microscopy (SEM) was used to reveal the morphology of sintered pellets in a JEOL JSM IT300 electron microscope. These images were acquired from polished samples and from fractured specimens.

2.3. Fracture toughness measurements

Fracture toughness was measured by a Vickers-indentation method using 1.5 mm thick specimens polished to colloidal silica finish. The specimens were indented at a load of P = 49 N for 15 s. The fracture-toughness value was calculated using the following two equations

$$K_{IC} = 0.016\left(\frac{E}{H_V}\right)^{0.5}\left(\frac{P}{C^{1.5}}\right) \quad (1)$$

$$K_{IFR} = 0.018\left(\frac{E}{H_V}\right)^{0.5}\left(\frac{P}{C^{1.5}}\right) \quad (2)$$

where E is the elastic modulus (MPa), Hv is the Vickers hardness (MPa) and C is half the radial crack length (m). The Hv value was determined from the elastic recovery of Vickers indentations, where the dimensions of the indentations introduced at 49 N were measured by an optical image analysis. The Young's modulus was measured by the nanoindentation technique (Ubi 1 nanoindenter, Hysitron) by considering the unloading process i.e. the elastic recovery.

2.4. Thermal characterization

The thermal expansion coefficient was measured in a high temperature thermodilatometer from room temperature to 1200 °C. Measurements were performed on samples of ~ 10 mm in length. The thermal conductivity was measured using the laser-flash method [30], where the thermal conductivity was calculated from specific heat capacity, thermal diffusivity and density

$$\lambda = D_{th} C_p \rho \quad (3)$$

where D_{th} is the thermal diffusivity, C_p the specific heat capacity and ρ is the density. The experiments were conducted using laser flash device (LFA 1000 Laser Flash Apparatus, Linseis Company) on disk-shaped carbon-coated samples of ~ 10 mm in diameter and 1 mm in thickness.

2.5. Optical characterization

The diffuse reflectance spectra measurements were recorded using an integrating sphere in the range of 200–1200 nm and performed in a 750 Perkin Elmer spectrophotometer.

Emission spectra were recorded in the range from 425 nm to 880 nm at room temperature, and in vacuum (0.5 Pa) and at room pressure (100 kPa), with an Ocean Optics USB4000 spectrometer fitted with a 3648-element linear silicon CCD array detector. The excitation source of light was provided by the laser diode power supply LDI-820 coupled with a Sheaumann Laser, Inc. diode laser emitting at 975 nm. A 900-nm short-pass filter was employed to block the signal of the laser. Samples were mounted in a Janis Research cryostat model RD, which was evacuated to attain the low pressure. The spectra were corrected for the wavelength dependent response of the spectrometer/detector system.

3. Results and discussion

3.1. Structural, microstructural and mechanical properties

The XRD results are shown in Fig. 1. The crystal structure of all samples can be indexed to the cubic fluorite-like lattice, the same crystal structure as the cubic ZrO_2 (PDF-30–1468). It is known that $Y_4Zr_3O_{12}$ can transform to rhombohedral upon long heat treatment process (must be maintained at 1300 °C or higher temperatures for several months [5,31]); but for example, in the case of application for TBCs, the operation temperature is at around 1200 °C, then it would require even longer time for the transformation to take place.

In order to establish, in a more quantitative way, the structural effect of the incorporation of Pr^{3+} and Yb^{3+} into the YZO, the XRD patterns were analyzed by the Rietveld refinement method. Additional details about space group, ionic coordinates and initial lattice parameter of the unit cell used for the Rietveld refinement analyses can be found in [19]. To compare experimental X-ray data with the calculated ones, a Rietveld refinement plot of sample YZO-Pr0.0105Yb1 is depicted in Fig. 2.

In Table 1 are presented the cell parameter and the average

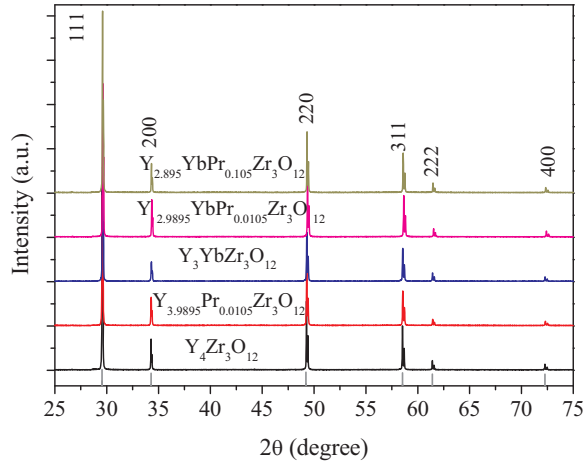

Fig. 1. X-ray diffraction patterns of the samples YZO-PrxYby sintered as pellets at 1550 °C for 2 h. The vertical lines correspond to the adapted reference pattern PDF-30-1468. Miller indices of planes associated with each maximum are given on the top.

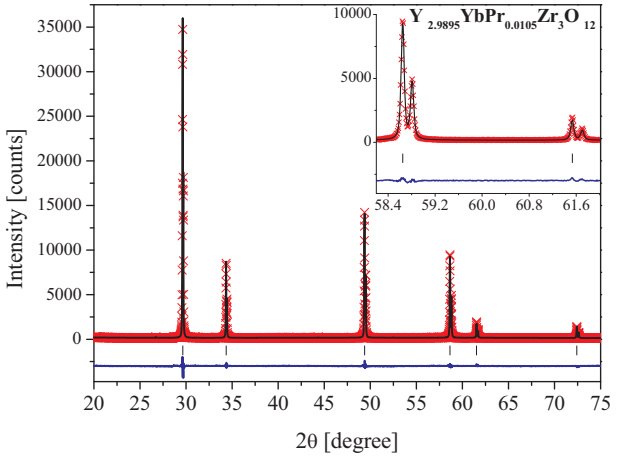

Fig. 2. Rietveld refinement plot of the sample YZO-Pr0.0105Yb1. The scatter crosses and the upper solid line correspond to the experimental and calculated data, respectively. The lower curve is the difference between calculated and measured diffraction patterns. Marks on the bottom represent the Bragg reflections associated with the cubic fluorite-like crystal phase. In the inset is shown the two-theta range from 58.2° to 62.0° where maxima associated with planes (311) and (222) appear.

Table 1
Lattice parameter and average crystallite size for all the YZO-PrxYby compositions.

Sample	a (Å)	Average crystallite size (nm)
$Y_4Zr_3O_{12}$	5.22803(2)	626(5)
$Y_{3.9895}Pr_{0.0105}Zr_3O_{12}$	5.22855(3)	480(5)
$Y_3YbZr_3O_{12}$	5.21617(4)	468(7)
$Y_{2.9895}YbPr_{0.0105}Zr_3O_{12}$	5.21629(2)	585(3)
$Y_{2.895}YbPr_{0.105}Zr_3O_{12}$	5.21996(2)	630(7)

crystallite size for each composition. Assuming a cubo-octahedral coordination for the cations, and according to [32], the ionic radii for Zr^{4+}, Yb^{3+}, Y^{3+} and Pr^{3+} are 0.84 Å, 0.985 Å, 1.019 Å and 1.126 Å, respectively. The cell parameter for each composition, is consistent with those ionic radii. If the cell parameter of the YZO sample is taken as a reference, it is observed an increase in the cell parameter when Pr^{3+} is incorporated in the sample YZO-Pr0.0105, even when this amount of Pr^{3+} represents only 0.15 mol% among all the cations present for this composition. On the other hand, the incorporation of Yb^{3+}, which is smaller in size than Y^{3+}, results in the reduction of the cell parameter for the sample YZO-Yb1. Intermediate, but accordant with the Pr^{3+} content, are the cell parameter values for compositions YZO-Pr0.0105Yb1 and YZO-Pr0.105Yb1 containing both, Pr^{3+} and Yb^{3+}.

Regarding the average crystallite size, first a reduction in the size is observed when only Pr^{3+} or only Yb^{3+} is added, but an increase when Pr^{3+} and Yb^{3+} are simultaneously added.

In Fig. 3 the SEM images of some fractured sintered samples are observed. The crystal size is around 1 μm for all compositions. Also, some porosity is observed in sintered pellets even when they were sintered at such high temperature as 1550 °C, which is advantageous for TBC application [33]. Moreover, the measured densities for all compositions were between 77% and 92.4% (of the theoretical density). This degree of densification is moderate considering that commonly hot or hot isostatic pressing is used to get almost theoretical densities in such compositions [33,34]. In Fig. 3e, a Vickers indentation is shown, it was done applying 49 N, and from this, the indentation size and the cracks generated were measured for obtaining the fracture toughness. This process was repeated for all compositions.

The results for fracture toughness calculated with Eqs. (1) and (2) are shown in Table 2. This property, describing mechanical resistance to thermal and stress cycling, is one of the most important issues when considering materials as possible candidates for TBCs along with low thermal conductivity. The values obtained in this study are similar to or slightly higher than those for YSZ and silica doped YSZ [35], TiO_2 and Al_2O_3-TiO_2 [36], and a just slightly lower than those values reported for ceria-alumina toughened YSZ [37].

3.2. Thermal properties

The thermal conductivity as a function of temperature for the investigated compositions are shown in Fig. 4; as it can be seen, it is almost temperature independent. All the compositions have remarkable low thermal conductivities, and are comparable with those reported for the pure $Y_4Zr_3O_{12}$ (YZO) base-composition, YSZ, YAG, and other zirconates [30,38–40]. The lowest thermal conductivity reported for undoped YZO is 2 W/m K at around 600 °C [34], and for pyrochlore zirconates and YSZ they are in the range from 1.2 W/m K to 3.0 W/m K [38,41]. It is important to underline that in our case, porosity could aid to get such low values as those showed in Fig. 4. For example, in porous YSZ, a porosity around 20% results in a decrease of around 30% in the thermal conductivity [38].

It is well known that for YSZ, the low thermal conductivity is due to the scattering of phonons by oxygen vacancies and other defects, as well as oxygen vacancy "hopping" [38]. The $Y_4Zr_3O_{12}$ (YZO) system in fact can be considered as an oxygen deficient zirconia ($Zr_{3/7}Y_{4/7}O_{2-2/7}$); so, the exceptionally low thermal conductivity can be attributed to the high concentration of oxygen vacancies [7]. Moreover, the lowest thermal conductivity was observed for those samples doped with Yb^{3+} only, or Yb^{3+} and small amount of Pr^{3+}. Then, it can be inferred that mass disorder has a major contribution. This is because the phonon scattering is enhanced when the difference in atomic mass of dopants increases [34].

The thermal expansion coefficient measured for all the samples is reported in Table 3. These values are on the same order of magnitude as those reported in yttria stabilized zirconia for compositions up to 10 mol% of Y_2O_3 and other materials [42,43]. According to the previous mechanical and thermal properties, all the compositions could be used as materials for thermal barriers.

3.3. Optical properties

In Fig. 5 reflectance spectra of the all samples are shown. Interesting to notice is the presence of a well-defined band from 850 nm to

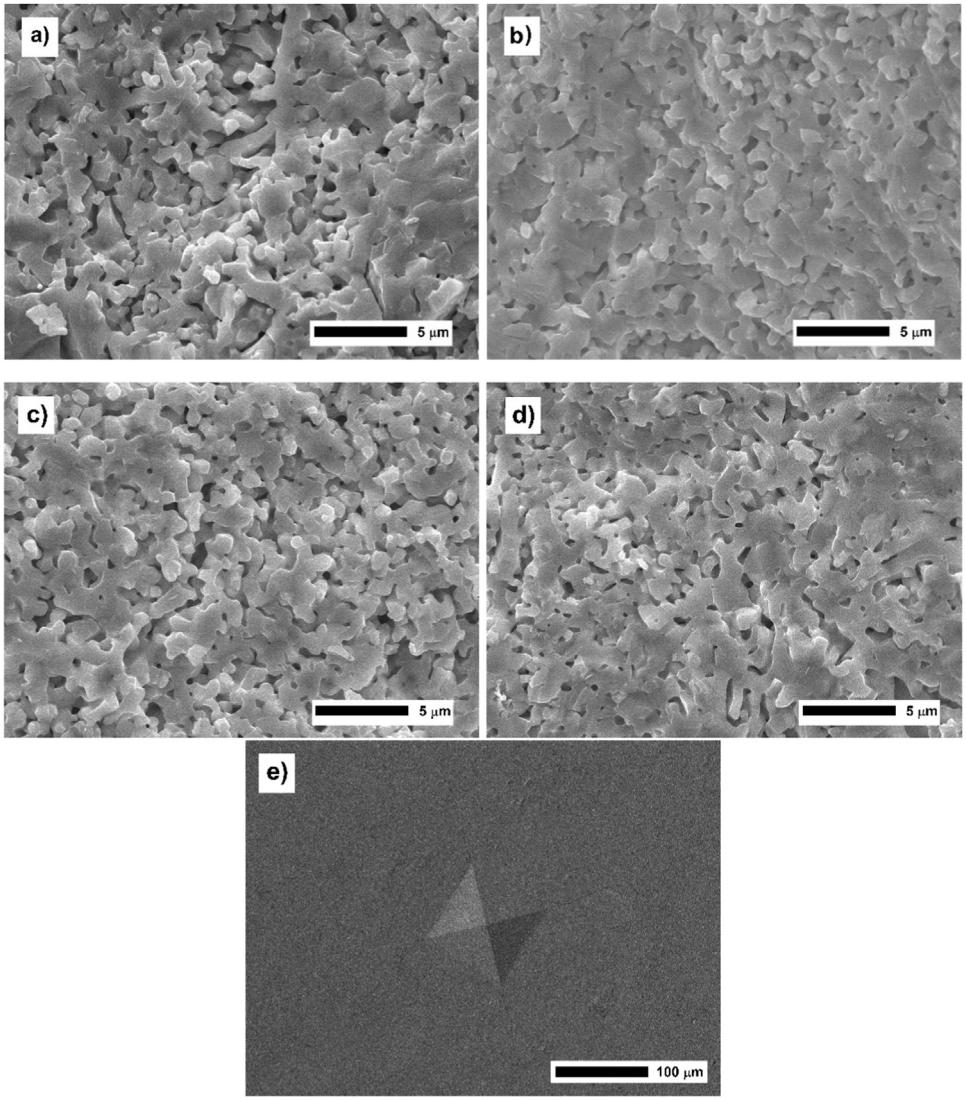

Fig. 3. SEM images of YZO-PY ceramics sintered at 1550 °C for 2 h: a) YZO, b) YZO:Pr0.0105, c) YZO:Pr0.0105Yb1, d) and e) YZO:Yb1.

Table 2
Fracture toughness calculated with Eqs. (1) and (2) for YZO-PY ceramics.

Sample	K_{IC} (MPa $m^{0.5}$)	K_{IFR} (MPa $m^{0.5}$)
$Y_4Zr_3O_{12}$	2.0506 ± 0.1242	2.3069 ± 0.1397
$Y_{3.9895}Pr_{0.0105}Zr_3O_{12}$	1.9040 ± 0.1296	2.1420 ± 0.1459
$Y_3YbZr_3O_{12}$	1.7717 ± 0.2870	1.9932 ± 0.3228
$Y_{2.9895}YbPr_{0.0105}O_{12}$	1.9769 ± 0.3625	2.2240 ± 0.4078
$Y_{2.895}YbPr_{0.105}O_{12}$	1.7309 ± 0.0559	1.9473 ± 0.0629

1000 nm in samples containing Yb^{3+}, it is ascribed to the transition $^2F_{7/2} \rightarrow {}^2F_{5/2}$ of that ion. However, no evidence of the presence of Pr^{3+} is observed in the reflectance spectra; a probable reason for this, is the oxidation of Pr^{3+} to Pr^{4+}. Supporting this fact, is the color of the samples since those ones that do not contain Pr ion have a white color, but those ones that do contain it, have an orange color which is accentuated by increasing the Pr concentration. Thus, the noticeable broad band from 200 nm to 600 nm exhibited in the reflectance spectra of the sample $YZOPr_{0.105}Yb$ is assigned to the O^2-Pr^{4+} ligand-to-metal charge transfer state (LMCT). This association is supported by previous reports about the optical properties of ZrO_2 and other zirconates doped with Pr [44,45]. Judging by their color, this O^2-Pr^{4+} LMCT state should be also present in the other samples containing Pr, but it is reasonable

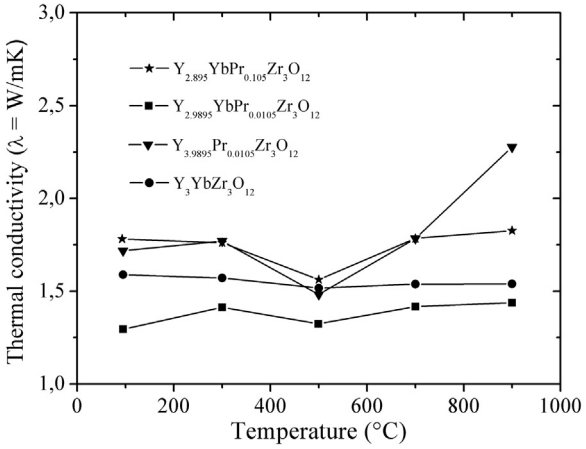

Fig. 4. Thermal conductivity of YZO-PY sintered ceramics at 1550 °C for 2 h.

to think that such a broad and intense band is not observed so conspicuously in their reflectance spectra because they have ten times less praseodymium ions as compared with those the sample YZOPr0.105Yb has.

To determine if the samples could produce white light under laser

Table 3
Thermal expansion coefficient of sintered pellets (at 25–1200 °C).

Sample	α (10^{-6}/°K)
$Y_4Zr_3O_{12}$	7.300 ± 0.034
$Y_{3.9895}Pr_{0.0105}Zr_3O_{12}$	7.542 ± 0.030
$Y_3YbZr_3O_{12}$	7.869 ± 0.039
$Y_{2.9895}YbPr_{0.0105}O_{12}$	9.182 ± 0.041
$Y_{2.895}YbPr_{0.105}O_{12}$	9.160 ± 0.040

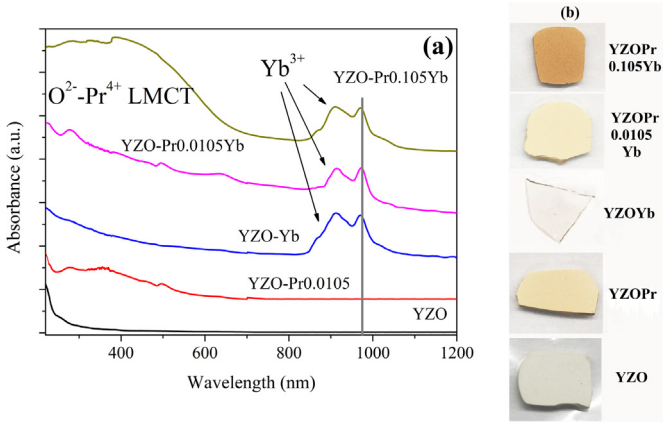

Fig. 5. Diffuse reflectance spectra (a) and pictures of the YZO-PrxYby pellets. The vertical line in (a) corresponds to the wavelength of the 975-nm laser.

irradiation, all the pellets were irradiated with a 975-nm laser. Surprisingly, although other samples have the same Yb concentration, and despite this phenomenon has been observed in undoped powder oxides made of nanocrystallites [8–11], only the pellet corresponding to the $Y_3YbZr_3O_{12}$ composition shows white light emission. In the cases of the undoped YZO and the YZO-Pr0.0105 samples, we explain the absence of the white light emission because there is no means to incorporate energy into the system as it is, when Yb^{3+} absorbs the radiation of the 975-nm laser (see Fig. 5). For those samples co-doped with ytterbium and praseodymium, the reasons are not clear at all, but we will propose an explanation later.

Fig. 6(a) shows the emission spectra of that pellet in vacuum at ~ 0.5 Pa. The spectra are taken consecutively, first starting at low laser irradiance and increasing the irradiance in steps up to 877 W/cm^2, and then decreasing the laser irradiance, following the same values as when the irradiance is increased. As previously observed [19], the intensity of emission increases as the wavelength increases, and similarly an increase in the integrated intensity of the emitted WL as the laser irradiance increases. The drop-in signal at ~ 890 nm is due to the cut-off filter employed for blocking the laser signal. In accordance with previous results [17,19] a hysteresis effect is also observed, but less pronounced than that one observed in Yb^{3+}-doped $Y_4Zr_3O_{12}$ powders made of nanocrystallites [19]. This result is consistent with the fact that less microstructural modifications induced by the laser irradiation, and which are thought as responsible for the hysteresis effect, are expected in sintered pellets in comparison with those present in powders.

The white-light is produced not only at vacuum but also at room pressure (~ 101 kPa), as it is seen in Fig. 6(b). However, the irradiance threshold for its generation is larger than the one needed when pellet is in vacuum. From Fig. 6(a) and (b) the observed irradiance thresholds at vacuum and at room pressure are 409 W/cm^2 and 707 W/cm^2, respectively. These values are even higher than those reported for the Yb^{3+}-doped $Y_4Zr_3O_{12}$ powders, which are 173 W/cm^2 and 223 W/cm^2, for samples having average crystallite sizes of 7 nm and 26 nm, respectively. But what is certainly surprising is that the powders have one hundred times less Yb^{3+} with respect to the pellet [19].

On the other hand, and in a similar way as it has been described previously [17], for the lower laser irradiances, namely, 85 W/cm^2 and 196 W/cm^2 (see Fig. 6(a)), for the pellet in vacuum, and 85 W/cm^2, 196 W/cm^2 and 303 W/cm^2 (see Fig. 6(a)) for the pellet at room pressure, the Yb^{3+} emission is present and its intensity increases as the irradiance increases, but it seems that at higher irradiances a "delocalization" process arises since the energy absorbed by the Yb^{3+} ions is no longer located at them, but it spreads throughout the bulk because the Yb^{3+} emission is significantly reduced [19]. This process, finally, gives place to the continuous WL emission. In this regard, the integrated intensity of the emission spectra for the YZO-Yb pellet shown in (Fig. 6c) accounts for the whole process. First, both plots show an increase in the emission intensity as the laser irradiance rises. If the irradiance increases even more, a decrement in emission is observed, and after reaching a minimum as the irradiance continues rising, the intensity increases and the white light starts to be emitted (see inset Fig. 6(c)). Although both curves present similar trends, higher laser irradiances are required for the pellet at room pressure to produce comparable intensity to the pellet in vacuum. In particular, it is observed that the intensity of the white light, when the pellet is irradiated at the highest laser's irradiance, differs noticeably. This effect can also be seen in the pictures shown in Fig. 6(d) and (e).

Following the previously reported approach [13,19,20], we fit the white light spectra using the Planck's law of blackbody radiation. To achieve the fitting between the white light emission spectra and the Planck's law, the only parameter is the absolute temperature. Fig. 7 shows plots of that temperature as a function of the irradiance of the laser. As it is seen, the value of the temperature at the same irradiances of the laser depends on the pressure, which is always higher for sample in vacuum. These differences are attributed to the significance of the modes of heat transfer involved in each pressure condition. While at room pressure, convection and conduction between the pellet and the surrounding air are present, which do not participate in vacuum. Therefore, given a irradiance laser, in vacuum the temperature of the system would be expected to be higher when compared to at atmospheric pressure, just as it is observed in Fig. 7. Also, it should be noticed that the temperature increases linearly with the laser irradiance in all cases when the pellet is at room pressure and for laser irradiances higher than 563 W/cm^2 when the pellet is in vacuum. This linear trend has been observed before in nanosized systems [19,20].

The fact that white light is not observed in samples containing both Yb and Pr is intriguing, but we can hypothesize some explanation about this result, which also could provide insight into the process that leads to the emission of the white light. When Pr^{3+} is oxidized to Pr^{4+}, acceptor levels are formed within the host band gap [46]. The fingerprint of these acceptor states is the presence in the reflectance spectra of Fig. 5 of the O^2-Pr^{4+} LMCT broad band. On the other hand, it has been established a relationship between the white light and the photocurrent generated under IR laser irradiation in graphene [47] and Yb-doped yttrium aluminum garnet [48]. Thus, whatever process leads to the generation of white light, the evidence suggests that an electronic contribution is important for the emergence of this phenomenon. In this sense, we can speculate that, in insulator materials, some participation should have the electrons of the valence band, since the creation of acceptor states would have an impact on the dynamics of such electrons when they gain energy.

All the previous results concerning the response of the samples under the IR laser irradiation complement the knowledge about the production of white light when Yb^{3+}-doped insulators are irradiated with IR lasers because: 1) Yb^{3+} allows the incorporation of energy into the system by absorbing the laser which ultimate leads to the white light (thermal radiation) emission, 2) it is demonstrate that the generation of white light is also possible in bulk ceramic oxides, and 3) that the introduction of additional electronic states, in this case associated with the Pr, inhibits the generation of the white light.

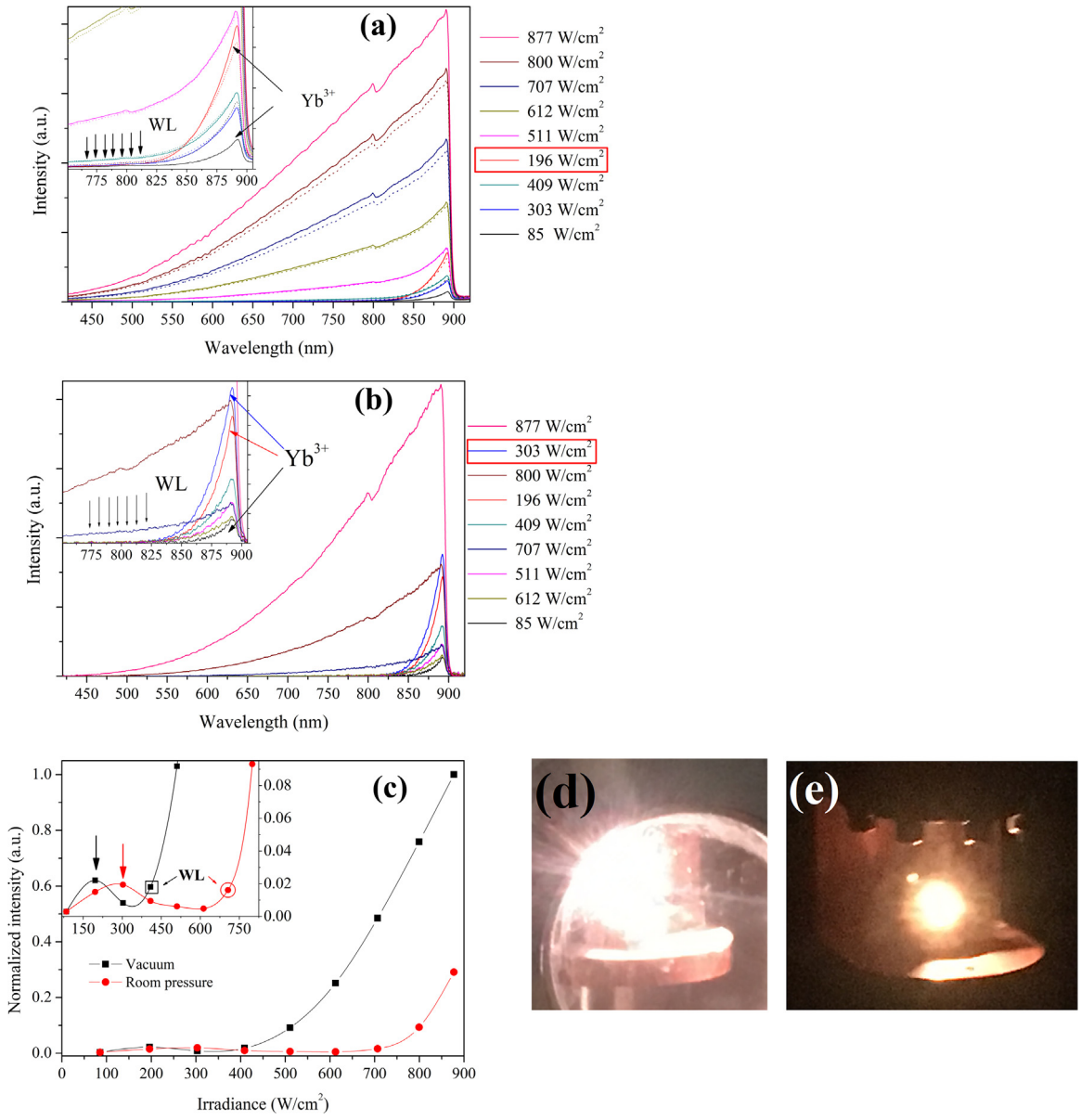

Fig. 6. Emission spectra of the pellet $Y_3YbZr_3O_{12}$ for different laser irradiances at vacuum (a) and at room pressure (b). In (a) the laser irradiance is first increased (solid lines) in steps until reaching a maximum (877 W/cm^2) and then it decreases (dotted line) to reach again the same values as those used when the irradiance is increased until it finally reaches the lowest irradiance value (85 W/cm^2). In (b) only spectra when the irradiance of the laser is increased are shown. The enclosed irradiance value on the right in (a) and (b) corresponds to the higher one at which the Yb^{3+} emission is still observed, for higher irradiances WL starts to be dominant (see text for further explanation). In the inset, emission spectra for lower irradiances are shown. Arrows pointing down indicate (continuous) emission for the lower laser irradiance (409 W/cm^2 vacuum, 707 W/cm^2 room pressure) at which white light starts to be observed. Normalized intensity is presented in (c) for vacuum and room pressure. Pictures of the white light emitted for the pellet in vacuum (d) and at room pressure (e) when the irradiance of the laser is 877 W/cm^2.

4. Conclusions

$Y_4Zr_3O_{12}$ bulk ceramics doped with Yb^{3+} and (nominally) Pr^{3+} were synthesized by the polymerizable complex method and sintered as pellets at 1550 °C for 2 h. All the specimens exhibit cubic fluorite- like crystal structure. The average crystallite size estimated by Rietveld analysis for all samples was around 0.5 μm, and confirmed by SEM. Regarding the thermal properties of the ceramics, it was found that thermal conductivity values were even below those reported for some YSZ, while the thermal expansion coefficient was in the same order as in the YSZ and other thermal insulator materials. The measured fracture toughness values seem promising because they are only slightly below those known for common compounds used as thermal barrier coatings. Concerning the optical properties, diffuse reflectance spectra show the presence of Pr^{4+}, which results from the oxidation of the originally added Pr^{3+}. Under a 975-nm laser irradiation, interestingly, only the sample doped with Yb^{3+} showed white light emission, originated from thermal radiation. In the undoped YZO and the YZO-Pr0.0105 samples, this finding is explained because there is no way to absorb the radiation of the 975-nm laser. In samples co-doped with Pr and Yb, the absence of white light generation seems to be related to the presence of acceptor levels within the band gap of the host, and ascribed to the Pr^{4+}. In summary, our results are important for the following reasons: 1) as far as we now, there is no previous reports about the production of white light in bulk ceramic oxides under NIR laser irradiation, 2) since no white light generation is observed in the undoped sample, it is reasonable to assume that defects and porosity should play an important role in favoring the white light generation in undoped powder oxides,

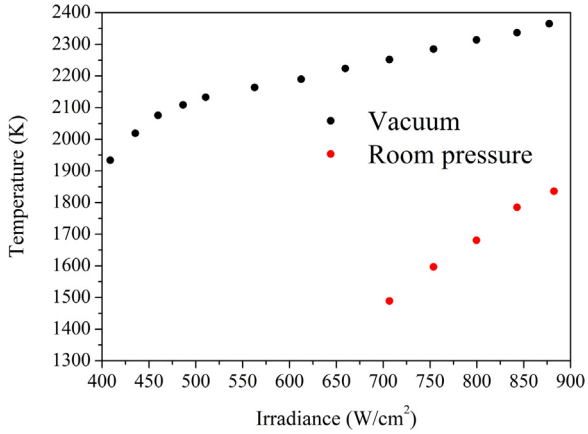

Fig. 7. Temperature as a function of laser irradiance for the pellet YZO-Yb in vacuum and at room pressure.

and 3) due to the fact that the introduction of additional electronic states within the band gap, in this case associated with the Pr^{4+}, inhibits the generation of white light, it is possible to speculate that electrons in the valence band participate in the emergence of the white light production in insulators materials.

Acknowledgments

Federico González thanks the support of CONACyT-México (CVU 89843–472353) for the sabbatical year at Boston College. The authors acknowledge to Laboratorio Divisional de Difracción de Rayos X (T-128) UAM-I México for XRD measurements. Also, we are grateful to Orlando Hernández-Cristobal (ENES-Morelia) for the SEM images.

References

[1] N. Mahato, A. Banerjee, A. Gupta, S. Omar, K. Balani, Progress in material selection for solid oxide fuel cell technology: a review, Prog. Mater. Sci. 72 (2015) 141–337.
[2] D.R. Clarke, S.R. Phillpot, Thermal barrier coating materials, Mater. Today 8 (2005) 22–29.
[3] X.Q. Cao, R. Vassen, D. Stoever, Ceramic materials for thermal barrier coatings, J. Eur. Ceram. Soc. 24 (2004) 1–10.
[4] M. Chen, B. Hallstedt, L.J. Gauckler, Thermodynamic modeling of the ZrO_2–$YO_{1.5}$ system, Solid State Ion. 170 (2004) 255–274.
[5] H.G. Scott, The yttria-zirconia δ-phase, Acta Cryst. B33 (1977) 281–282.
[6] S.P. Ray, V.S. Stubican, Fluorite related ordered compounds in the ZrO_2-CaO and ZrO_2-Y_2O_3 systems, Mater. Res. Bull. 12 (1977) 549–556.
[7] P.K. Schelling, S.R. Phillpot, Mechanism of thermal transport in zirconia and yttria-stabilized zirconia by molecular-dynamics simulation, J. Am. Ceram. Soc. 84 (2001) 2997–3007.
[8] G. Bilir, G. Ozen, M. Bettinelli, F. Piccinelli, M. Cesaria, B. Di Bartolo, Broadband visible light emission from nominally undoped and Cr^{3+} doped garnet nanopowders, IEEE Photonics J. 6 (2014) 2201211.
[9] G. Bilir, B. Di Bartolo, Production of bright, wideband white-light from Y_2O_3 nanopowders induced by laser diode emission, Opt. Mater. 36 (2014) 1357–1360.
[10] M. Erdem, G. Eryurek, B. DiBartolo, White light emission from sol–gel derived γ-Y2Si2O7nanoparticles, J. Alloy. Compd. 639 (5) (2015) 483–487.
[11] S. Tabanli, H. Cinkaya Yilmaz, G. Bilir, M. Erdem, G. Eryurek, B. Di Bartolo, J. Collins, Broadband white light emission from doped and undoped insulators, ECS J. Sol. State Sci. 7 (1) (2018) R3199–R3210.
[12] A.K. Singh, S. Singh, D. Kumar, D.K. Rai, S.B. Rai, K. Kumar, Light-into-heat conversion in La_2O_3:Er^{3+}-Yb^{3+} phosphor: an incandescent emission, Opt. Lett. 37 (2012) 776–778.
[13] J. Wang, T. Ming, Z. Jin, J. Wang, L.D. Sun, C.H. Yan, Photon energy upconversion through thermal radiation with the power efficiency reaching 16%, Nat. Commun. 5 (2014) 5669.
[14] Y. Zhu, W. Xu, C. Li, H. Zhang, B. Dong, L. Xu, S. Xu, H. Song, Broad white-light and infrared emission bands in YVO_4: Yb^{3+}, Ln^{3+} (Ln^{3+} = Er^{3+}, Tm^{3+}, or Ho^{3+}), Appl. Phys. Express 5 (2012) 092701.
[15] W. Strek, L. Marciniak, P. Gluchowski, D. Hreniak, Infrared laser stimulated broadband white emission of Yb:YAG nanoceramics, Opt. Mater. 35 (2013) 2013–2017.
[16] G. Bilir, J. Ozen, M. Collins, Cesaria, B. Di, Bartolo, Unconventional production of bright white light emission by Nd-doped and nominally undoped Y_2O_3 nanopowders, IEEE Photonics J. 6 (4) (2014) 8200518.
[17] S.M. Redmond, S.C. Rand, S.L. Oliveira, Bistable emission of a black-body radiator, Appl. Phys. Lett. 85 (2004) 5517–5519.
[18] S.M. Redmond, S.C. Rand, X.L. Ruan, M. Kaviany, Multiple scattering and nonlinear thermal emission of Yb^{3+} and Er^{3+}:Y_2O_3 nanopowders, J. Appl. Phys. 95 (8) (2004) 4067–4077.
[19] F. González, R. Khadka, R. López-Juárez, J. Collins, B. Di Bartolo, Emission of white-light in cubic $Y_4Zr_3O_{12}$:Yb^{3+} induced by a continuous infrared laser, J. Lumin. 198 (2018) 320–326.
[20] M.L. Debasu, D. Ananias, I. Pastoriza-Santos, L.M. Liz-Marzán, J. Rocha, L.D. Carlos, All-in-one optical heater-thermometer nanoplatform operative from 300 to 2000 K based on Er^{3+} emission and blackbody radiation, Adv. Mater. 25 (2013) 4868–4874.
[21] W. Strek, L. Marciniak, D. Hreniak, A. Lukowiak, Anti-Stokes bright yellowish emission from $NdAlO_3$ nanocrystals, J. Appl. Phys. 111 (2012) 024305.
[22] W. Strek, L. Marciniak, A. Bednarkiewicz, A. Lukowiak, R. Wiglusz, D. Hreniak, White emission of lithium ytterbium tetraphosphate nanocrystals, Opt. Express 19 (2011) 14083.
[23] J. Wang, J.H. Hao, P. Tanner, Persistent luminescence upconversion for Er_2O_3 under 975 nm excitation in vacuum, J. Lumin. 164 (2015) 116–122.
[24] J. Wang, J.H. Hao, P. Tanner, Luminous and tunable upconversion for YAG ($Yb_3Al_5O_{12}$) and $(Yb,Y)_2O_3$ nanopowders, Opt. Lett. 35 (23) (2010) 3922–3924.
[25] J. Wang, P.A. Tanner, Upconversion for white-light generation by a single compound, J. Am. Chem. Soc. 132 (2010) 947–9490.
[26] X. Chen, W. Xu, Y. Zhu, P. Zhou, S. Cui, L. Tao, L. Xua, H. Song, Nd_2O_3/Au nanocomposites: upconversion broadband emission and enhancement under near-infrared light excitation, J. Mater. Chem. C 2 (2014) 5857–5863.
[27] R.W. Cheary, A.A. Coelho, A fundamental parameters approach to X-ray line-profile fitting, J. Appl. Crystallogr. 25 (1992) 109–121.
[28] D. Black, D. Windover, A. Henins, J. Filliben, J. Cline, Certification of standard reference material 660B, Nat. Inst. Stand. Technol. 26 (2011) 155–158.
[29] M. Järvinen, Application of symmetrized harmonics expansion to correction of the preferred orientation effect, J. Appl. Crystallogr. 26 (1993) 525–531.
[30] H. Lehmann, D. Pitzer, G. Pracht, R. Vassen, D. Stoever, Thermal conductivity and thermal expansion coefficients of the lanthanum rare-earth-element zirconate system, J. Am. Ceram. Soc. 86 (2003) 1338–1344.
[31] T.A. Lee, A. Navrotsky, I. Molodetsky, Enthalpy of formation of cubic yttria-stabilized zirconia, J. Mater. Res. 18 (2003) 908–918.
[32] R.D. Shannon, Revised effective ionic radii and systematic studies of interatomic distances in halides and chalcogenides, Acta Cryst. A32 (1976) 751–767.
[33] R. Vassen, X. Cao, F. Tietz, D. Basu, D. Stoever, Zirconates as new materials for thermal barrier coatings, J. Am. Ceram. Soc. 83 (2000) 2023–2028.
[34] M.R. Winter, D.R. Clarke, Oxide materials with low thermal conductivity, J. Am. Ceram. Soc. 90 (2007) 533–540.
[35] K. Hiraga, K. Morita, B.-N. Kim, Y. Sakka, Fracture toughness of yttria-stabilized cubic zirconia (8Y-CSZ) doped with pure silica, Mater. Trans. 45 (2004) 3324–3329.
[36] D. Chicot, G. Duarte, A. Tricoteaux, B. Jorgowski, A. Leriche, J. Lesage, Vickers Indentation Fracture (VIF) modeling to analyze multi-cracking toughness of titania, alumina and zirconia plasma sprayed coatings, Mater. Sci. Eng. A 527 (2009) 65–76.
[37] R.V. Mangalaraja, B.K. Chandrasekhar, P. Manohar, Effect of ceria on the physical, mechanical and thermal properties of yttria stabilized zirconia toughened alumina, Mater. Sci. Eng. A 343 (2003) 71–75.
[38] K.W. Schlichting, N.P. Padture, P.G. Klemens, Thermal conductivity of dense and porous yttria-stabilized zirconia, J. Mater. Sci. 36 (2001) 3003–3010.
[39] A.M. Limarga, S. Shian, R.M. Leckie, C.G. Levi, D.R. Clarke, Thermal conductivity of single- and multi-phase compositions in theZrO_2–Y_2O_3–Ta_2O_5 system, J. Eur. Ceram. Soc. 34 (2014) 3085–3094.
[40] Y.J. Su, R.W. Trice, K.T. Faber, H. Wang, W.D. Porter, Thermal conductivity, phase stability, and oxidation resistance of $Y_3Al_5O_{12}$ (YAG)/Y_2O_3–ZrO_2 (YSZ) thermal-barrier coatings, Oxid. Met. 61 (2004) 253–271.
[41] J. Wu, X. Wei, N.P. Padture, P.G. Klemens, M. Gell, E. García, P. Miranzo, M.I. Osendi, Low-thermal-conductivity rare-earth zirconates for potential thermal-barrier-coating applications, J. Am. Ceram. Soc. 85 (2002) 3031–3035.
[42] H. Hayashi, T. Saitou, N. Maruyama, H. Inaba, K. Kawamura, M. Mori, Thermal expansion coefficient of yttria stabilized zirconia for various yttria contents, Solid State Ion. 176 (2005) 613–619.
[43] R. Vaßen, M.O. Jarligo, T. Steinke, D.E. Mack, D. Stöver, Overview on advanced thermal barrier coatings, Surf. Coat. Technol. 205 (2010) 938–942.
[44] N. Van Vugt, T. Wigmans, G. Blasse, Electron transfer spectra of some tetravalent lanthanide ions in ZrO2, J. Inorg. Nucl. Chem. 35 (1973) 2601–2602.
[45] H.E. Hoefdraad, Charge-transfer spectra of tetravalent lanthanide ions in oxides, J. Inorg. Nucl. Chem. 37 (1975) 1917–1921.
[46] J.J. Kim, S.R. Bishop, Di Chen, H.L. Tuller, Defect chemistry of Pr doped ceria thin films investigated by in situ optical and impedance measurements, Chem. Mater. 29 (2017) 1999–2007.
[47] W. Strek, R. Tomala, M. Lukaszewicz, B. Cichy, Y. Gerasymchuk, P. Gluchowski, L. Marciniak, A. Bednarkiewicz, D. Hreniak, Laser induced white lighting of graphene foam, Sci. Rep. 7 (2017) 41281.
[48] M. Łukaszewicz, W. Stręk, Co-occurrent white emission and photoconductivity in Yb3+ doped YAG nanoceramics induced by infrared laser excitation, J. Lumin. 199 (2018) 251–257.